Pré-Publicações do Departamento de Matemática
Universidade de Coimbra
Preprint Number 18–52

ON THE ACCURATE SIMULATION OF NEARSHORE AND DAM BREAK PROBLEMS INVOLVING DISPERSIVE BREAKING WAVES

JOSÉ S. ANTUNES DO CARMO, JOSÉ A. FERREIRA AND LUÍS PINTO

Abstract: The ability of numerical models to deal with wave breaking processes and dry areas is of paramount importance for applications in coastal zones and dam breaks. The mathematical models commonly used in such real problems are usually based on Boussinesq-type equations and, to a small extend, on Serre equations. However, these standard models are weakly dispersive and must be appropriately modified to deal with breaking waves and dry areas. Indeed, nearshore and dam break problems involve complex wave dynamics and highly dispersive wave processes can easily arise. In those cases, it is well known that weakly dispersive models like the ones based on classical Boussinesq or Serre equations are unreliable for an accurate simulation of the phenomena involved.

In this work we extend the applicability of an improved Serre model, herein denoted by Serre$_{\alpha,\beta}$, to include the wave breaking process, the broken waves propagation, and dry areas. We provide a comprehensive set of numerical examples involving wave propagation over exposed and submerged structures, as well as dam break problems. The numerical experiments show the accuracy and robustness of the proposed model. Particular attention is given to bottom friction modeling, where the standard Manning's assumption is compared with a more realistic formulation. Also noteworthy is the simulation of wave breaking problems with highly dispersive effects. The advantages of the Serre$_{\alpha,\beta}$ model over the standard Serre model for these challenging cases are clear.

Keywords: Extended Serre equations; Saint-Venant equations; Dispersive waves; Breaking waves; Improved bottom friction; Wave-structure interaction.

1. Introduction

Accurate simulation of water waves propagation is very important in the coastal regions management. One relevant example is the wave's interaction with seawalls or underwater bars. These are structures build near the coast that have the function of protecting it against coastal erosion and flooding. Another context in which water wave models play a crucial role is in the

Received November 26, 2018.

This work was partially supported by the Centre for Mathematics of the University of Coimbra - UID/MAT/00324/2013, funded by the Portuguese Government through FCT/MEC and co-funded by the European Regional Development Fund through the Partnership Agreement PT2020. Luís Pinto was also supported by FCT scholarship SFRH/BPD/112687/2015.

simulation of flooding due to dam breaking events. In both cases, an accurate simulation allows not only the design of more efficient structures, but also the prevention and mitigation of hazards.

In order to deal with the complex nearshore water dynamics, a coastal model must be able to reproduce wave breaking and dry areas. Most of the approaches for wave breaking consist in the introduction of additional dissipative terms in existing wave's models. The role of these terms is to account for the decay of the water wave height inside the breaking region. Strategies to localize the breaking point are also required. In addition, the presence of dry areas means that we need to consider bottom friction effects. This brings additional numerical challenges since the friction term is stiff and dominant in dry or almost dry regions. In these conditions it is also important to use numerical schemes that have the positivity preserving property.

Another important aspect is the presence of dispersive and nonlinear effects. Wave dispersion strength is measured by the parameter $\varrho = h_0/l$, where h_0 is the reference depth and l the wavelength. The nonlinearity strength is measured by $\epsilon = a/h_0$, with a the typical wave amplitude. It is well known that nearshore wave dynamics is strongly nonlinear [2]. This is particularly true at the end of the shoaling zone and also in the surf and swash zones. As the wave shoals up a slope and in very shallow water conditions, it steepens accumulating higher harmonics (dominant nonlinearity) that are released on wave breaking or on a downslope (dominant dispersive effects). After this process, the wave can eventually recover producing an irregular pattern, more or less complex. It is important to highlight that in the literature dispersive effects are usually analyzed separately from breaking, see, e.g., [16] and references therein. In this work, we show that a complete model must include simultaneously nonlinearity, wave breaking, and dispersive effects. Moreover, dispersion is so relevant, that models with weakly dispersive properties are not accurate enough.

Numerical models that solve the Saint-Venant equations [12], the Boussinesq equations [4], and the Serre or Green & Naghdi equations [41] are commonly used in coastal wave modeling. These models can be classified based on their dispersion and nonlinear properties. The Saint-Venant equations are weakly nonlinear and non-dispersive, i.e., some nonlinear terms and all terms of dispersive origin are ignored. Therefore, the Saint-Venant equations are suitable for wave propagation in the breaking zone. The Boussinesq equations are weakly dispersive and weakly nonlinear, i.e., it is assumed that

$\epsilon \ll 1$ and $\varrho \ll 1$. Due to these properties the standard Boussinesq equations have a limited applicability for nearshore applications. Several modifications to the Boussinesq equations have been proposed. For example, in [32, 52, 36], the dispersive properties were improved by adding terms of dispersive origin and in [53, 21], fully nonlinear Boussinesq-type models are presented. The standard Serre equations, like Boussinesq, are weakly dispersive, however, they are also fully nonlinear.

Despite being fully nonlinear Serre equations are inadequate for breaking zones. The problem is that near breaking points a singularity appears and the assumptions made to derive the equations are invalid [2]. To overcome this limitation some recent studies have proposed a hybrid approach [49, 39, 20, 31]. Since shock discontinuities are well resolved by Saint-Venant, this approach portrays breaking waves as shock waves and in the breaking zone a switch from Serre to Saint-Venant is made. Other limitation of the standard Serre equations is the weak dispersivity. This is a significant drawback for complex wave dynamics and several modifications have been proposed to overcome it [14, 52, 21, 6, 31, 10]. For example, following the approach used in [32] for Boussinesq, dispersion characteristics were improved in [14] considering additional terms of dispersive origin. An efficient numerical scheme to solve this improved Serre system, denoted Serre$_{\alpha,\beta}$, was recently presented in [16].

The goal of this paper is to extend the Serre$_{\alpha,\beta}$ model to include wave breaking and dry regions. By doing so, we obtain an accurate model covering all the nearshore wave processes. The relevance of improved dispersion properties is highlighted. This paper is organized as follows. In Section 2 we briefly deduce the Serre$_{\alpha,\beta}$ model. Following [16], we write the model in a decoupled dispersive-hyperbolic form suitable for numerical implementation. Next, in Section 3, we present the strategies used to embed wave breaking and bottom friction. Here, we deviate from the standard Manning's assumption and use a more realistic formulation for friction. The numerical scheme is presented in Section 4. We propose a hybrid approach combining finite volume and finite difference. Numerical experiments are given in Section 5 and we finish in Section 6 with some conclusions.

2. The Serre$_{\alpha,\beta}$ Model

As illustrated in Figure 1, we consider the one-dimensional horizontal case and represent by $b(x)$ the time constant bathymetry, by $u(x,t)$ the flow

velocity, and by $h(x,t) = h_0 + \eta(x,t) - b(x)$ the water height, with $\eta(x,t)$ the free surface elevation and h_0 the reference depth. Here, x is the spatial variable and t is the time variable.

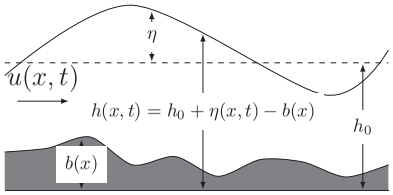

FIGURE 1. Sketch of the domain and main notation.

Following [16, 17] the one-dimensional version of the classical Serre equations with bottom friction can be written in the following compact form

$$\begin{cases} h_t + (hu)_x = 0 \\ (I + hT_{\frac{1}{h}})((hu)_t + (hu^2 + \frac{1}{2}gh^2)_x + ghb_x) - hT(g\eta_x) + hQ(u) = -\frac{\sigma}{\rho}, \end{cases} \tag{1}$$

where g is the gravitational acceleration, I is the identity operator, Q is defined by

$$Q(v) = h(2h_x + b_x)(v_x)^2 + \frac{4}{3}h^2 v_x v_{xx} + hb_{xx} v v_x + (\eta_x b_{xx} + \frac{h}{2}b_{xxx})v^2 \tag{2}$$

and $T_{\frac{1}{h}} = T(\frac{v}{h})$ with T given by

$$T(v) = -\frac{h^2}{3}v_{xx} - hh_x v_x + (b_x\eta_x + \frac{h}{2}b_{xx})v. \tag{3}$$

Still in (1), at the right-hand side of the momentum equation we have the friction term $-\sigma/\rho$, with ρ the fluid density and σ the friction at the bottom.

To obtain an efficient numerical scheme for Serre system (1) we use a splitting approach to decouple the dispersive and nonlinear terms. Let $S(t)$ be the solution operator of (1) and let us assume for now that

$$S(t) = S_d(t) \circ S_{nl}(t) \tag{4}$$

where $S_{nl}(t)$ is the solution operator associated with the nonlinear part

$$\begin{cases} h_t + (hu)_x = 0 \\ (hu)_t + (hu^2 + \frac{1}{2}gh^2)_x + ghb_x = -\frac{\sigma}{\rho}, \end{cases} \tag{5}$$

[39] V. Roeber and K. F. Cheung. Boussinesq-type model for energetic breaking waves in fringing reef environment. *Coast. Eng.*, 70:1–20, 2012.
[40] V. Roeber, K. F. Cheung, and M. H. Kobayashi. Shock-capturing Boussinesq-type model for nearshore wave processes. *Coast. Eng.*, 57:407–423, 2010.
[41] F. Serre. Contribution à l'étude des écoulements permanents et variables dans les canaux. *Houille Blanche*, 8:374–388, 1953.
[42] M. Siddique, T. Merabtene, and Y. Tajima. Wave transformation and hydrodynamic characteristics of wave-breaking models coupled with Boussinesq equations. *J. Hydraul. Res.*, 55:759–771, 2017.
[43] J. F. A. Sleath. Velocities and shear stresses in wave-current flows. *J. Geophys. Res.*, 96:15237–15244, 1991.
[44] I. Svendsen, J. Veeramony, J. Bakunin, and J. Kirby. The flow in weak turbulent hydraulic jumps. *J. Fluid Mech.*, 418:25–57, 2000.
[45] I. A. Svendsen and P. A. Madsen. A turbulent bore on a beach. *J. Fluid Mech.*, 148:73–96, 1984.
[46] C. E. Synolakis. The runup of solitary waves. *J. Fluid Mech.*, 185:523–545, 1987.
[47] H. Tanaka and A. Thu. Full-range equation of friction coefficient and phase difference in a wave-current boundary layer. *Coast. Eng.*, 22:237–254, 1994.
[48] M. Tissier, P. Bonneton, F. Marche, F. Chazel, and D. Lannes. A new approach to handle wave breaking in fully non-linear Boussinesq models. *Coast. Eng.*, 67:54–66, 2012.
[49] M. Tonelli and M. Petti. Hybrid finite-volume finite-difference scheme for 2DH improved boussinesq equations. *Coast. Eng.*, 56:609–620, 2009.
[50] A. Watanabe and M. Dibajnia. A numerical model of wave deformation in surf zone. In *Proceedings of the 21st international conference on coastal engineering*, pages 578–587, 1988.
[51] A. Watanabe and K. Maruyama. Numerical modeling of nearshore wave field under combined refraction, diffraction and breaking. *Coast. Eng. J.*, 29:193–213, 1986.
[52] G. Wei and J. T. Kirby. Time-dependent numerical code for extended Boussinesq equations. *J. Waterw. Port. C-ASCE*, 121:251–261, 1995.
[53] G. Wei, J. T. Kirby, S. T. Grilli, and R. Subramanya. A fully nonlinear boussinesq model for surface waves. Part 1. Highly nonlinear unsteady waves. *J. Fluid Mech.*, 294:71–92, 1995.
[54] C. Zhang, Q. Zhang, J. Zheng, and Z. Demirbilek. Parameterization of nearshore wave front slope. *Coast. Eng.*, 127:80–87, 2017.
[55] Y. Zhang, A. B. Kennedy, A. S. Donahue, J. J. Westerink, and N. Panda. Rotational surf zone modeling for $o(\mu^4)$ Boussinesq-Green-Naghdi systems. *Ocean Model.*, 79:45–53, 2014.
[56] C. Zoppou, J. Pitt, and S. G. Roberts. Numerical solution of the fully non-linear weakly dispersive serre equations for steep gradient flows. *Appl. Math. Model.*, 48:70–95, 2017.

JOSÉ S. ANTUNES DO CARMO
IMAR, DEP. OF CIVIL ENGINEERING, UNIVERSITY OF COIMBRA, PORTUGAL
E-mail address: jsacarmo@dec.uc.pt

JOSÉ A. FERREIRA
CMUC, DEP. OF MATHEMATICS, UNIVERSITY OF COIMBRA, PORTUGAL
E-mail address: ferreira@mat.uc.pt

LUÍS PINTO
CMUC, DEP. OF MATHEMATICS, UNIVERSITY OF COIMBRA, PORTUGAL
E-mail address: luisp@mat.uc.pt

[18] J. S. A. do Carmo, F. J. Seabra-Santos, and A. B. Almeida. Numerical solution of the generalized serre equations with the McCormack finite-difference scheme. *Int. J. Numer. Meth. Fl.*, 16:725–738, 1993.
[19] J. S. A. do Carmo, A. Temperville, and F. J. Seabra-Santos. Bottom friction and time-dependent shear stress for wave-current interaction. *J. Hydraul. Res.*, 41:27–37, 2010.
[20] M. Filippini, A. G. Kazolea, and M. Ricchiuto. A flexible genuinely nonlinear approach for nonlinear wave propagation, breaking and runup. *J. Comput. Phys.*, 310:381–417, 2016.
[21] M. F. Gobbi, J. T. Kirby, and G. Wei. A fully nonlinear Boussinesq model for surface waves. Part 2. Extension to O(kh^4). *J. Fluid Mech.*, 405:181–210, 2000.
[22] S. Gottlieb, C.-W. Shu, and E. Tadmor. Strong stability-preserving high-order time discretization methods. *SIAM Rev.*, 87:89–112, 2001.
[23] S. H.-Thanh and A. Temperville. A numerical model of the rough turbulent boundary layer in combined wave and current interaction. In *Sand Transport in Rivers, Estuaries and the Sea*, pages 93–100, 1991.
[24] S.-C. Hsiao and T.-C. Lin. Tsunami-like solitary waves impinging and overtopping an impermeable seawall: Experiment and RANS modeling. *Coast. Eng.*, 57:1–18, 2010.
[25] M. Kazolea, A. I. Delis, and C. E. Synolakis. Numerical treatment of wave breaking on unstructured finite volume approximations for extended Boussinesq-type equations. *J. Comput. Phys.*, 271:281–305, 2014.
[26] M. Kazolea and M. Ricchiuto. On wave breaking for Boussinesq-type models. *Ocean Model.*, 123:16–39, 2018.
[27] A. B. Kennedy, Q. Chen, J. T. Kirby, and R. A. Dalrymple. Boussinesq modelling of wave transformation, breaking and runup. I: 1D. *J. Waterw. Port C-asce.*, 126:39–48, 2000.
[28] G. Kesserwani and Q. Liang. RKDG2 shallow-water solver on non-uniform grids with local time steps: Application to 1D and 2D hydrodynamics. *Appl. Math. Model.*, 39:1317–1340, 2015.
[29] G. Th. Klonaris, C. D. Memos, and Th. V. Karambas. A Boussinesq-type model including wave-breaking terms in both continuity and momentum equations. *Ocean Eng.*, 57:128–140, 2013.
[30] A. Kurganov and G. Petrova. A second-order well-balanced positivity preserving central-upwind scheme for the Saint-Venant system. *Commun. Math. Sci.*, 5:133–160, 2007.
[31] D. Lannes and F. Marche. A new class of fully nonlinear and weakly dispersive Green-Naghdi models for efficient 2D simulations. *J. Comput. Phys.*, 282:238–268, 2015.
[32] P. A. Madsen, R. Murray, and O. R. Sørensen. A new form of the Boussinesq equations with improved linear dispersion characteristics. *Coast. Eng.*, 15:371–378, 1991.
[33] R. Manning. On the flow of water in open channels and pipes. *Transactions of the Institution of Civil Engineers of Ireland*, 20:161–207, 1891.
[34] M. W. Morris. *CADAM Concerted Action on Dambreak Modelling*. Report SR 571, HR Wallingford, 2000.
[35] National Tsunami Hazard Mitigation Program (NTHMP). *Proceedings and Results of the 2011 NTHMP Model Benchmarking Workshop. Boulder: U.S. Department of Commerce/ NOAA/NTHMP; NOAA Special Report. p. 436*. 2012.
[36] O. Nwogu. Alternative form of Boussinesq equations for nearshore wave propagation. *J. Waterw. Port. C-ASCE*, 119:618–638, 1993.
[37] J. P. A. Pitt, C. Zoppou, and S. G. Roberts. Behaviour of the Serre equations in the presence of steep gradients revisited. *Wave Motion*, 76:61–77, 2018.
[38] R. R. Reinnauer and W. H. Hager. Non-breaking undular hydraulic jump. *J. Hydraul. Res.*, 33:683–704, 1995.

and $S_d(t)$ is the solution operator of the dispersive part

$$\begin{cases} h_t = 0 \\ (I + hT_{\frac{1}{h}})((hu)_t) - hT(g\eta_x) + hQ(u) = 0. \end{cases} \tag{6}$$

We observe that system (5) corresponds to the classical Saint-Venant system with friction at bottom level.

To obtain the proposed Serre$_{\alpha,\beta}$ system we follow [14] and add and subtract to the momentum equation of (6) the term

$$hT^{\alpha,\beta}_{\frac{1}{h}}((hu)_t),$$

with

$$T^{\alpha,\beta}(v) = -\beta\frac{h^2}{3}v_{xx} - \alpha h h_x v_x + \alpha(b_x\eta_x + \frac{h}{2}b_{xx})v. \tag{7}$$

Using also the classical approximation $u_t = -g\eta_x$ and the fact that $h_t = 0$ we get

$$\begin{cases} h_t = 0 \\ (I + hT_{\frac{1}{h}} + hT^{\alpha,\beta}_{\frac{1}{h}})((hu)_t) - h(T - T^{\alpha,\beta})(g\eta_x) + hQ(u) = 0. \end{cases} \tag{8}$$

Denoting the solution operator of (8) by $S^{\alpha,\beta}_d$ we define our Serre$_{\alpha,\beta}$ model as

$$S^{\alpha,\beta}(t) = S^{\alpha,\beta}_d(t) \circ S_{nl}(t). \tag{9}$$

Remark 2.1 Serre and the proposed Serre$_{\alpha,\beta}$ systems are equivalent up to order $O(\sigma^2)$ and the classical one is recovered when $\alpha = \beta = 0$.

Remark 2.2 Another well-known model [3] with improved dispersive properties can be obtained by setting

$$S^{\theta}(t) = S^{\theta}_d(t) \circ S_{nl}(t), \tag{10}$$

with $S^{\theta}_d(t)$ given by

$$\begin{cases} h_t = 0 \\ (I + h\theta T_{\frac{1}{h}})((hu)_t) - hT(g\eta_x) + hQ(u) = 0, \end{cases}$$

with $\theta \geq 0$. For non-breaking and non-friction problems with strong dispersive effects it was shown in [16] that the proposed model (9) offers noticeable

improvements over (10). Naturally, the advantages over traditional Serre (1) are even more significant.

3. Wave Breaking and Bottom Friction Modeling

In this section we discuss the strategies adopted to model wave breaking and bottom friction. These two features are crucial in any coastal wave model. We start by explaining how breaking is embedded in Serre$_{\alpha,\beta}$.

3.1. Wave Breaking. When a wave approaches the shoreline the water depth decreases and the wave becomes very step. Simultaneously, the crest velocity increases, and when it exceeds the overall wave velocity the crest breaks and separates from the wave. This turbulent phenomenon, characterized at large scales by strong energy dissipation and wave height reduction, is called wave breaking. Equations specifically designed for turbulent behavior, e.g., RANS (Reynolds-Average Navier-Stokes), have been employed to simulate this process [24]. However, due to the heavy computational cost, depth-averaged equations, such as Serre, are still preferred. The problem is that these equations are invalid in the breaking zone and they need to be complemented with wave breaking methodologies.

Most of the available techniques are based on local *ad-hoc* dissipative terms. These terms are added to the wave model (e.g., Serre or Boussinesq-type equations), with the goal of capturing energy dissipation in the breaking zone. The popular eddy viscosity approach [27] considers the term

$$D_{hu} = \partial_x(\nu(hu)_x), \tag{11}$$

where ν is the so-called eddy viscosity. The term (11) is to be added at the wave models momentum equation. In our case, the second equation of (1). The major criticism to this approach is the lack of physical meaning of the parameters used to express the eddy viscosity. In order to obtain a better aproximation some authors have used k-l turbulent models [36, 26, 55]. In general the eddy viscosity is written using the Prandtl and Kolmogorov relation, which assumes that ν can be written as a product of a turbulent kinetic energy (k) and a turbulent length scale (l). The several approaches differ in the way that k and l are calculated. For example, in [26], l is assumed proportional to the water height h and k is the solution of a partial differential equation.

The model proved to be efficient and robust. The second group is particularly challenging and innovating since it involves wave breaking and dispersive effects. These complex examples reveal the limitations of classical Serre system and highlight the advantage of our improved Serre system.

References

[1] S. Beji and J. A. Battjes. Experimental investigation of wave propagation over a bar. *Coast. Eng.*, 19:151–162, 1993.

[2] P. Bonneton, E. Barthelemy, F. Chazel, R. Cienfuegos, D. Lannes, F. Marche, and M. Tissier. Recent advances in Serre-Green Naghdi modelling for wave transformation, breaking and runup processes. *Eur. J. Mech. B Fluids*, 30:589–597, 2011.

[3] P. Bonneton, F. Chazel, D. Lannes, F. Marche, and M. Tissier. A splitting approach for the fully nonlinear and weakly dispersive Green-Naghdi model. *J. Comput. Phys.*, 230:1479–1498, 2011.

[4] J. Boussinesq. Théorie des ondes et des remous qui se propagent le long d'un canal rectangulaire horizontal. *J. Math. Pures Appl.*, 2:55–108, 1872.

[5] M. Brocchini, M. Drago, and L. Iovenitti. The modelling of short waves in shallow waters comparison of numerical models based on boussinesq and serre equations. *Coastal Engineering Proceedings*, 1(23):76–88, 2011.

[6] F. Chazel, D. Lannes, and F. Marche. Numerical simulation of strongly nonlinear and dispersive waves using a Green-Naghdi model. *J. Sci. Comput.*, 48:105–116, 2011.

[7] A. Chertock, S. Cui, A. Kurganov, and T. Wu. Steady state and sign preserving semi-implicit Runge-Kutta methods for odes with stiff damping term. *SIAM J. Numer. Anal.*, 53:2008–2029, 2015.

[8] A. Chertock, S. Cui, A. Kurganov, and T. Wu. Well-balanced positivity preserving central-upwind scheme for the shallow water system with friction terms. *Int. J. Numer. Meth. Fl.*, 78:355–383, 2015.

[9] R. Cienfuegos, E. Barthélemy, and P. Bonneton. A wave-breaking model for Boussinesq-type equations including mass-induced effects. *J. Waterw. Port C-asce.*, 136:10–26, 2010.

[10] D. Clamond, D. Dutykh, and D. Mitsotakis. Conservative modified Serre-Green-Naghdi equations with improved dispersion characteristics. *Commun. Nonlinear Sci.*, 45:245–257, 2017.

[11] W. Dally and C. Brown. A modeling investigation of the breaking wave roller with application to cross-shore currents. *J. Geophys. Res.*, 100(C12):24873–24883, 1995.

[12] B. de Saint-Venant. Theory of unsteady water flow, with application to river floods and to propagation of tides in river channels. *French Acad. Sci.*, 73:148–154, 237–240, 1971.

[13] R. Deigaard and J. Fredsøe. Shear stress distribution in dissipative water waves. *Coast. Eng.*, 13:357–378, 1989.

[14] J. S. A. do Carmo. Boussinesq and Serre type models with improved linear dispersion characteristics: Applications. *J. Hydraul. Res.*, 51:719–727, 2013.

[15] J. S. A. do Carmo. Natural responses to changes in morphodynamic processes caused by human action in watercourses: A contribution to support management. *Int. J. Disaster Risk Reduct.*, 24:109–118, 2017.

[16] J. S. A. do Carmo, J. A. Ferreira, L. Pinto, and G. Romanazzi. An improved Serre model: Efficient simulation and comparative evaluation. *Appl. Math. Model.*, 56:404–423, 2018.

[17] J. S. A. do Carmo and F. J. Seabra-Santos. On breaking waves and wave-current interaction in shallow water: A 2DH finite element model. *Int. J. Numer. Meth. Fl.*, 22:429–444, 1996.

capable of reproduce the experimental data with good accuracy. The limitations of Serre are clearly evident at the last gauge located at $x = 17$ (m). During the shoaling phase the wave accumulates higher harmonics that are released as highly dispersive waves during the breaking phase and on the downward slope. Therefore, the last gauge is the most challenging since the higher harmonic are already fully released. At the gauges of Figure 18 Serre and Serre$_{\alpha,\beta}$ have a similar behavior.

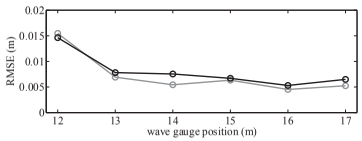

FIGURE 21. Comparison of the RMSE at the six gauges of the Beji et al. (1993) experiment; Serre$^M_{\alpha,\beta}$ (black line) and Serre$_{\alpha,\beta}$ (grey line).

The comparison between Serre$^M_{\alpha,\beta}$ and Serre$_{\alpha,\beta}$ is given in Figure 21. It shows that Serre$_{\alpha,\beta}$ results in a somewhat lower RMSE at all gauges except the first one.

6. Conclusion

In this paper we propose, implement, and test a complete wave model for nearshore and dam break simulation. Our approach is based on a Serre system with improved dispersion properties. We complement this system with a wave breaking methodology and friction terms.

For breaking we follow a well established strategy that consists in ignoring all the dispersive terms in the neighborhood of a breaking wave. This strategy takes advantage of our splitting scheme that separates the model in a hyperbolic part and a dispersive part. A high order positivity preserving finite volume method is used to discretize the hyperbolic part and finite difference are used to discretize the dispersive part. For friction we propose a more physically based alternative to the usual Manning formula. The numerical results suggest that the proposed formulation is more accurate than the one based in Manning.

Our model is tested against several experimental problems. We separate the problems in two groups: weakly dispersive waves and highly dispersive waves. In the first group we focus on the breaking and friction methodologies.

In [9], the authors used energy principles to claim that a more physically sounded model is obtained when an additional term is also added to the continuity equation. The proposed model is based on the two breaking terms

$$D_h = \partial_x(d_h h_x), \tag{12}$$

$$D_{hu} = \partial_x(d_{hu}(hu)_x), \tag{13}$$

where (13) is included in the momentum equation and (12) is the extra term that appears in the continuity equation. Exploiting arguments developed in [11, 13, 44] the authors also suggest expressions for the functions d_h and d_{hu}. Basically, they are of exponential type, centered around the moving wave crest and dependent on the local still water depth. Estimates for the parameters involved are also given.

Let us also mention the friction-type wave breaking models, which are based on terms of the form $f_d u$, with f_d a dissipation function dependent on h [51, 50, 17]. The rationale behind this approach is that energy dissipation due to wave breaking can be related to surface friction. Finally, we refer the roller-type models [45, 5, 13], based on terms of type R_x, with R a function that depends on u and h. This physically solid approach relies on the concept of "surface-roller", the air-water mixing region formed in front of the breaking wave. In this context, energy dissipation occurs due to friction between the wave and the roller. In both models the extra terms are included in the momentum equation.

A numerical comparison against experimental data was performed in [42] using eddy viscosity [36], roller [5], and friction [50] models. It was concluded that the three models were equally accurate at predicting wave height. In [9], the numerical experiments favored the proposed model (based on (12)-(13)) over the eddy viscosity model given in [27]. In both cases the authors used Boussinesq-type equations.

In this work we adopt a different wave breaking strategy. Our approach, presented for the first time in [49], consists is switching locally from Serre$_{\alpha,\beta}$ to the Saint-Venant system when the wave is about to break. The motivation is to explore the splitting strategy (9) presented in Section 2. Recall that Serre$_{\alpha,\beta}$ is decoupled in a dispersive part $S_d^{\alpha,\beta}(t)$ and a nonlinear part $S_{nl}(t)$ which is exactly the Saint-Venant system. Therefore, breaking can be easily incorporated by simply ignoring the contribution from the dispersive term $S_d^{\alpha,\beta}(t)$. This methodology has proven to be efficient and has gained

considerable popularity [25, 20, 31, 48, 26, 49]. This technique is also physically meaningful. In fact we can see breaking waves fronts as shocks and it is well known that the Saint-Venant system admit shock waves solutions that dissipate energy. Morevoer, it doesn't requires additional *ad-hoc* dissipative terms. Naturally, like the models previously presented, this is still a limited view of the complex wave breaking phenomenon.

In [26], this hybrid strategy was compared with a eddy viscosity model using Serre and Boussinesq-type equations. The numerical results suggest that the performance of the two strategies is identical. One drawback of the hybrid approach is the appearance of numerical instabilities when the switch is made, particularly for fine meshes. We refer that similar issues occur, e.g., in some eddy viscosity models when the diffusive terms are activated [27]. Here, we achieve a smooth transition by using the sigmoidal function

$$f(t) = \frac{1}{1+\exp(-4(10t-1))}, \quad t \geq 0.$$

A different approach, where the transition is embedded as a kind of boundary condition is proposed in [20].

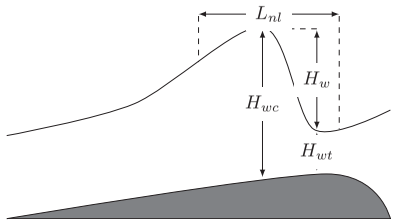

FIGURE 2. Definition sketch of a breaking wave and related variables.

Concerning breaking modeling we still need to present the mechanisms used to activate and deactivate the breaking process. There are several strategies and the optimal one is problem dependent [20, 25, 26, 48, 9, 29]. In this work, we consider that a wave starts to break when the front slope angle exceeds a predefined threshold, i.e.,

$$|\eta_x| \geq \phi_i. \tag{14}$$

For breaking termination we use one of following two conditions, the front slope angle satisfies

$$|\eta_x| \leq \phi_f, \tag{15}$$

between $\text{Serre}_{\alpha,\beta}$ and experimental data collected with three gauges placed at the bar crest. The results reveal that the wave shape is well captured by our model.

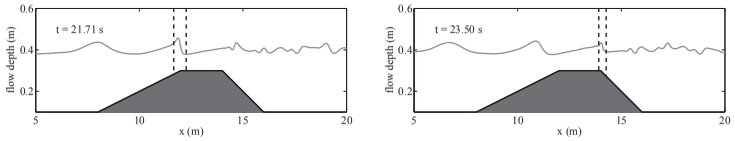

FIGURE 19. Snapshots of the flow propagation in the Beji et al. (1993) experiment; the area between the two dash lines corresponds to the breaking region.

Two snapshots of the wave are given in Figure 19. They show one of the first moments after a wave front begins to break, at $t = 21.71$ (s), and one of last moments before the wave front stops breaking, at $t = 23.50$ (s). These results reveal that our model correctly predicts the onset and duration of breaking.

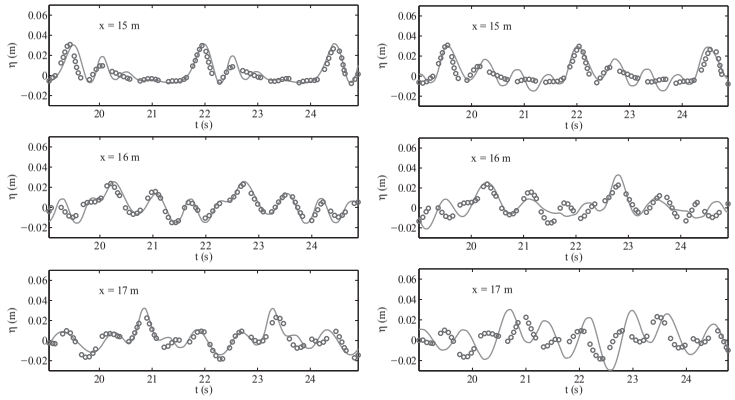

FIGURE 20. Comparison between numerical (solid line) and experimental data (dots) at the last three gauges. From left to right: $\text{Serre}_{\alpha,\beta}$ and classical Serre.

For the comparison between $\text{Serre}_{\alpha,\beta}$ and classical Serre we use the data recorded with three gauges placed after the bar crest. The results of the simulations are given in Figure 20. Unlike Serre, the proposed $\text{Serre}_{\alpha,\beta}$ is

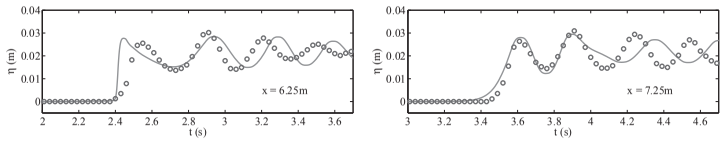

FIGURE 17. Comparison between the classical Serre model (solid line) and experimental data (dots) at the last two gauges used in the experiment of Carmo et al. (1993).

5.4. Beji et al. [1] **- Periodic wave propagation over a submerged bar.** Our last experiment deals with the propagation of a sinusoidal wave over a submerged bar [1]. The setup is illustrated in the top left image of Figure 18. It shows the bar with a front slope of 1:20 and a back slope of 1:10. The initial water height is $h_0 = 0.4$ (m), leaving the 0.3 (m) high bar completed submerged. The incident wave height is 0.027 (m), the frequency is 1/2.5 (s), and the wavelength is 4.7904 (m). This challenging case involves wave shoaling, wave breaking, and higher harmonic release.

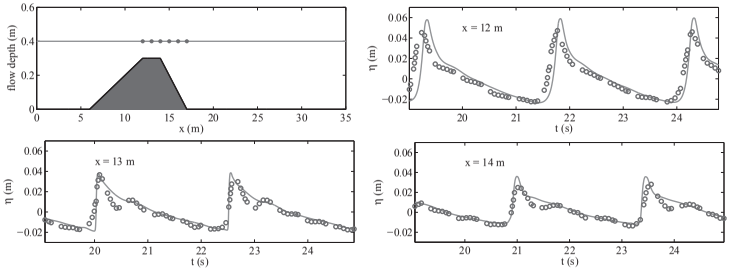

FIGURE 18. The figure in the top left corner shows a schematic representation of the setup used in the experiment of Beji et al. (1993). The horizontal gray line represents the initial still water depth, $h_0 = 0.4$ (m). The dots indicate the gauges positions. The remaing figures show a comparison between $\text{Serre}_{\alpha,\beta}$ (solid line) and experimental data (dots) at the first three gauges.

To simulate the incident wave we used an input condition at the left boundary [16]. The mesh size was set to $\Delta x = 0.015$ (m) and the breaking parameters were set to $\phi_i = 0.5$ and $F_f = 1.08$. We also defined $\alpha = 0.04$, $\beta = 0.07$, and the friction term $n_k = 0.02$. In Figure 18 we present the comparison

or the wave's Froude number (F) verifies $F \leq F_f$, with

$$F = \left(\frac{(2H_{wc}/H_{wt} + 1)^2 - 1}{8} \right)^{1/2} \tag{16}$$

and where H_{wc} and H_{wt} (see Figure 2)) are the water depth at the wave's crest and trough, respectively. We consider two breaking termination conditions because in some experimental tests one gives better results, or is more robust, than the other. For breaking initiation we found condition (14) accurate enough for all the experiments. The optimal values of ϕ_i, ϕ_f, and F_f depend on several aspects like, type of breaking model, forms of wave breaking (spilling, plunging, or surging), and employed numerical scheme.

Some efforts have been made in order to predict the optimal wave breaking parameters ϕ_i, ϕ_f, and F_f. One such case is [54] where, using extensive experimental data, the authors propose two empirical formulas for ϕ_i. One such formula expresses ϕ_i as a function of local wave parameters, while the other relates ϕ_i with the relative water depth and bed slope. The extensive data analyzed in that work also shows that ϕ_i can be in the range of 0.15 to 0.8. Note that condition (14) is based on the fact that when a wave approaches shallow waters the wave front angle increases and beyond a critical threshold the wave crest becomes unstable and breaks. The breaking termination condition (15) is closely related with the breaking initiation condition (14). Naturally, for the same experiment, the value ϕ_f must be lower than the one adopted for ϕ_i. Let us also note that (16) can be obtained from the ratio of conjugate depths in a hydraulic jump. In this sense the value $F = 1$ means that there is no jump and as F increases we observe a transition from a smooth undular jump to a undular jump characterized by shock waves and breaking phenomena. The application of Froude number to wave breaking is based on the relation between the increasing Froude number and the development of wave breaking mechanism in a hydraulic jump. Using this analogies some authors have estimated that the transition from non-breaking wave to breaking wave occurs for F equal 1.36 [38].

If a breaking wave is identified we also need to define the extension of the region, denoted L_{nl}, around the breaking point that is governed by $S_{nl}(t)$, i.e., the Saint-Venant system. The common practice is to use a value proportional to the wave front height, $L_{nl} = CH_w = C(H_{wc} - H_{wt})$, for $C > 1$. The value of C must be sufficient larger to avoid that non-physical dispersion effects influence the break region, we have set $C = 10$. In Figure 2 we give

an illustration of the notation used in the breaking model. The proposed methodology can be summarized as follows:

- If (14) is false; solve $S^{\alpha,\beta}(t) = S_d^{\alpha,\beta}(t) \circ S_{nl}(t)$.
- If (14) is true; a wave is breaking.
  Calculate L_{nl} and solve $S^{\alpha,\beta}(t) = S_{nl}(t)$ in L_{nl} and $S^{\alpha,\beta}(t) = S_d^{\alpha,\beta}(t) \circ S_{nl}(t)$ elsewhere.
- If (15) (or (16)) is false; the wave is still breaking.
  Calculate L_{nl} and solve $S^{\alpha,\beta}(t) = S_{nl}(t)$ in L_{nl} and $S^{\alpha,\beta}(t) = S_d^{\alpha,\beta}(t) \circ S_{nl}(t)$ elsewhere.
- If (15) (or (16)) is true; the wave stopped breaking.
  Solve $S^{\alpha,\beta}(t) = S_d^{\alpha,\beta}(t) \circ S_{nl}(t)$.

Naturally, more than one breaking point can be identified in the computational domain. In that case all the breaking wave fronts are followed and the breaking algorithm is applied to each one of them.

3.2. Bottom Friction. Bottom friction is a energy dissipation process consequence of the interaction between a viscous fluid (water) and a rough surface (sea-bottom). This process has a strong impact on erosion and sediment transport, two crucial aspects in coastal management. Friction is strongly influenced by several factors like sea-bottom roughness and morphology, water depth, and velocity. Another friction-inducting factor that is frequently overlooked by wave models is the current. This may not be relevant for laboratory experiments, but in real life applications any complete coastal model must take it into account. For instance, it is known that breaking waves, particularly surging breaking, induce strong currents in the surf zone.

In this work, we express bottom friction using the usual quadratic dependence on velocity, $\sigma/\rho = \tau_b u|u|$, with τ_b a friction coefficient. This parameterization can be seen as a particular case of the more general, $\tau_l u + \tau_t h u|u|$, with τ_l and τ_t laminar and turbulent coefficients, respectively.

Most of the formulations used to express τ_b are based on empirical laws. For example, from laboratory experiments with uniform turbulent flow in open-channel, Manning [33] presented the following law

$$S = \frac{n_k^2 u|u|}{R^{4/3}}, \tag{17}$$

where S is the open-channel slope, n_k is the so-called Manning's coefficient, related with the channel roughness, and R is the hydraulic radius, the ratio

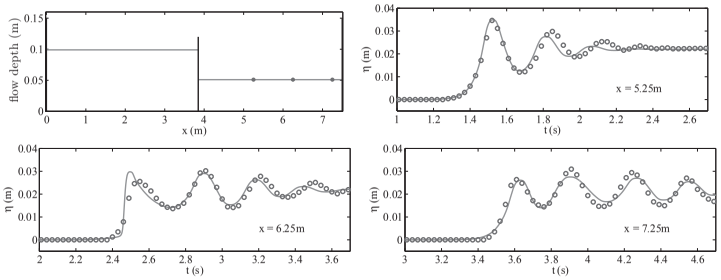

FIGURE 15. The figure in the top left corner shows a schematic representation of the setup used in the experiment of Carmo et al. (1993). The dots indicate the gauges positions. The remaing figures show a comparison between numerical (solid line) and experimental data (dots) at the three gauges.

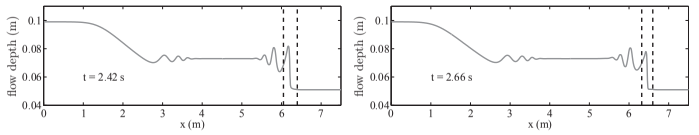

FIGURE 16. Snapshots of the simulated Carmo et al. (1993) experiment at two different times. The area between the dash lines corresponds to breaking regions.

0.04 and 0.1, respectively. For breaking we used $\phi_i = 0.43$ and $F_f = 1.32$, and we found the friction term to be negligible. The images of Figure 15 show that the numerical results are in close agreement with the laboratory data. The wave height is well predicted and no significant phase distortion is observed. Two wave snapshots at time $t = 2.42$ (s) and $t = 2.66$ (s) are given in Figure 16. They show the front wave breaking as reported in [18].

In Figure 17 we give the numerical results obtained with classical Serre at the last two gauges. Here the dispersive effects are more relevant and a significant phase discrepancy is observed. Note that the height of the breaking front wave is well predicted. This suggests that the differences observed are in fact due to the weakly dispersive properties of Serre. At the first gauge the results are similar to the ones obtained with Serre$_{\alpha,\beta}$.

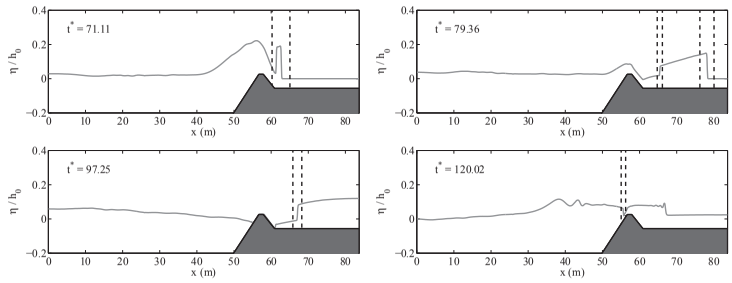

FIGURE 13. Snapshots of the soliary wave propagation in the Roeber et al. (2010) experiment; the area between two dash lines corresponds to breaking regions.

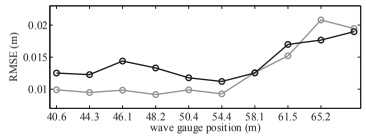

FIGURE 14. Comparison of the RMSE at the ten gauges of the Roeber et al. (2010) experiment; $\text{Serre}^{M}_{\alpha,\beta}$ (black line) and $\text{Serre}_{\alpha,\beta}$ (grey line).

5.3. Highly dispersive waves. In this section we illustrate the ability of our approach to deal with wave breaking and highly dispersive effects simultaneously. The goal is to highlight the superiority of the improved $\text{Serre}_{\alpha,\beta}$ over classical Serre. In the simulation of such type of processes, besides the breaking parameters, also the parameters α and β become relevant. For the experiments of this section we used F_f instead of ϕ_f for breaking termination.

5.3.1. *Carmo et al.* [18] - *Dam break flow over a wet and flat channel.* Our first test case is a laboratory dam break problem presented in [18]. As shown in the top left image of Figure 15, it consists of a reservoir with a gate located at $x = 3.8$ (m). The initial water depth upstream and downstream was 0.099 m and 0.051 m, respectively. The channel was open at the downstream end and closed at the upstream end. Three gauges were placed at the downstream portion of the channel.

To simulate this experiment we have used $\Delta x = 0.01$ (m) and the initial condition (28) with $\delta = 0.05$. The parameters α and β were set equal to

between the water area A and the wetted perimeter P. To realize how S is related with bottom friction let us consider a open-channel with bottom angle ζ and length L, and let us assume that the only forces are the water impelling force F_g, given by,

$$F_g = g\rho AL\sin(\zeta),$$

and the opposite resisting force F_b due to bottom friction,

$$F_b = \sigma PL.$$

Since the flow is uniform the two forces are of equal magnitude and we easily deduce

$$\sigma = g\rho R\sin(\zeta).$$

Using Manning's equation (17) to evaluate S, together with the usual approximation $R \approx h$ and the small-angle condition $\sin(\zeta) \approx S$, we get,

$$\frac{\sigma}{\rho} = g\frac{n_k^2}{h^{1/3}}u|u| = \tau_b u|u|. \tag{18}$$

The friction coefficient τ_b defined by (18) is the most widely used in the literature.

More well founded parameterizations can however be obtained. One such option is presented next. Following [17], we set

$$\frac{\sigma}{\rho} = \frac{1}{2}\tau_{cw}u|u|,$$

with τ_{cw} a coefficient that accounts for current (τ_c) and wave (τ_w) friction. Denoting by u_c the current velocity we define τ_{cw} by

$$\tau_{cw} = \frac{|u_c|}{|u_c|+|u|}\tau_c + \frac{|u|}{|u_c|+|u|}\tau_w.$$

This expression can be extended to accommodate the friction arising from the pressure gradient acting on the bottom roughness (τ_p). In this case, it reads

$$\tau_{cw} = \frac{|u_c|}{|u_c|+|u|}\tau_c + \frac{|u|}{|u_c|+|u|}(\tau_w + \tau_p).$$

Several expressions have been presented for the coefficients τ_c, τ_w, and τ_p. We adopt the ones of [19]. They are built on the work developed in [47, 23, 43], which is devoted to the analysis of a two-equation turbulent boundary layer

model of the k-l type [23]. For a single current and rough turbulent flow the suggest parameterizations are

$$\tau_c = \frac{k^2}{\left(\ln\left(\frac{h}{z_0}\right) - 1\right)^2}, \quad \tau_w = c_1 \exp\left(c_2 \left(\frac{K_N}{A}\right)^{c_3}\right), \quad \text{and} \quad \tau_p = c_4 \left(\frac{K_N}{A}\right),$$

with k the von Kármán's constant ($k = 0.4$), z_0 the roughness length ($z_0 = K_N/30$), $A = T|u|/2\pi$ with T the wave period, and c_i, $i = 1, \ldots, 4$, empirical coefficients. After experimental fitting they were set to $c_1 = 0.00140$, $c_2 = 4.5840$, and $c_3 = 0.1340$. Regarding c_4, it was set to 0.48 as given in [43]. For our laboratory like experiments we ignore current and pressure friction and we get term

$$\frac{\sigma}{\rho} = \frac{1}{2}\tau_w u|u| = \frac{1}{2} c_1 \exp\left(c_2 \left(\frac{K_N}{A}\right)^{c_3}\right) u|u|. \tag{19}$$

The optimal value of the parameter K_N is problem dependent. It is usually assumed [15] that K_N and n_k (the Manning's coefficient) are related by the equation

$$n_k = \frac{1}{21.1}\left(\frac{K_N}{2.5}\right)^{1/6}. \tag{20}$$

4. Numerical Scheme

The splitting strategy (9) decouples the proposed Serre$_{\alpha,\beta}$ model in a hyperbolic part $S_{nl}(t)$ and a dispersive part $S_d^{\alpha,\beta}(t)$. This separation allows us to use different methodologies suitable for each term. A brief description of our strategy is presented next.

4.1. Spatial Discretization. To solve the hyperbolic part we resort to the efficient high-order finite volume method presented in [8], see also [30]. This is a positivity-preserving scheme in the sense that preserves the positivity of water depth h. This crucial physical restriction brings additional challenges for the numerical methods particularly near dry or almost dry conditions, i.e., $h \sim 0$.

Let us consider the one-dimensional domain $\Omega = [x_L, x_R]$ and the uniform cell-centered finite volume mesh, $\bar{x}_{i+1} = \bar{x}_i + \Delta x$, $i = 1, \ldots, N-1$, with $\bar{x}_1 = x_L + \Delta x/2$ and $\bar{x}_N = x_R - \Delta x/2$. Let us also define $\bar{x}_{i\pm1/2} = \bar{x}_i \pm \Delta x/2$, $i = 1, \ldots, N$, with $\bar{x}_{1-1/2} = x_L$ and $\bar{x}_{N+1/2} = x_R$. Taking the friction term

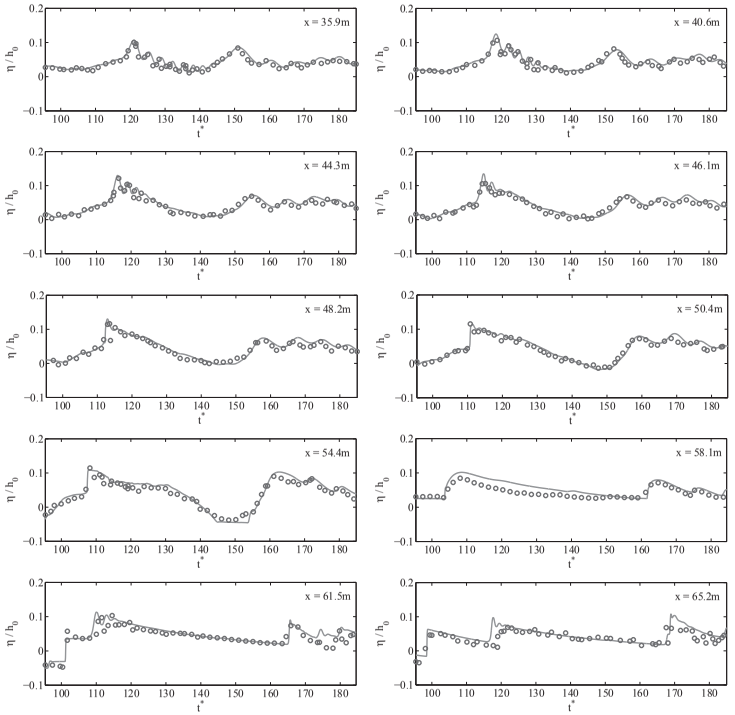

FIGURE 12. Comparison between numerical (solid line) and experimental data (dots) at the ten gauges of the Roeber et al. (2010) experiment.

seen at $t^* = 79.36$. At $t^* = 97.25$ the bore is already moving upstream after being reflected by the solid wall at the downstream end. By time $t^* = 120.02$ the bore has crossed the reef crest creating and hydraulic jump at the top of the outer reef. This wave dynamics is in accordance with the description presented in [40].

The comparison between Serre$^M_{\alpha,\beta}$ and Serre$_{\alpha,\beta}$ is given in Figure 14. Here, Serre$_{\alpha,\beta}$ is more accurate than the Manning based Serre$^M_{\alpha,\beta}$ at seven of the ten gauges. At the remaining three gauges Serre$^M_{\alpha,\beta}$ has a smaller RMSE in one of them, $x = 61.5$ (m), and the RMSE is identical at the other two, $x = 54.4$ (m) and $x = 65.2$ (m).

The initial condition for h is discontinuous across the dam location. To avoid numerical instabilities we use the expression

$$h(x,0) = h_d + \frac{h_u - h_d}{2}\left(1 + \tanh\left(\frac{x_g - x}{\delta}\right)\right), \tag{28}$$

where h_d and h_u are the water depth downstream and upstream, respectively, x_g is the gate location, and δ is a small positive parameter that we set equal to 0.1 [37].

5.2.3. *Roeber et al.* [40] - *Solitary wave propagating over an exposed reef.* In last example of this section we analyze the interaction of a solitary wave with an idealized fringing reef [40]. The experimental setup is shown in Figure 11. The outer reef has a slope of 1/12 and the still water depth of 2.5 (m) leaves the reef crest exposed by 6 (cm) and the reef flat submerged by 14 (cm) of water.

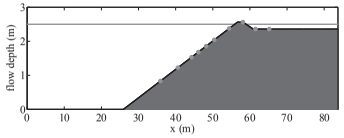

FIGURE 11. Schematic representation of the setup used in the experiment of Roeber et al. (2010). The horizontal gray line represents the initial still water depth, $h_0 = 2.5$ (m).

The solitary wave with amplitude $a/h_0 = 0.3$ and initially centered around $x_0 = 15$ (m), shoals over the outer reef and breaks just before the crest at around $t^* = 67$, with $t^* = t\sqrt{g/h_0}$. The flume is closed at both ends and a series of breaking and reflection events occur during the experiment. The comparison between the experimental data recorded at ten different gauges and the numerical simulation is depicted in Figure 12. The data starts at $t^* = 95.7$, after the first passage of the wave front by all the gauges. Overall, our model reproduces the experimental data with good accuracy. For later times, as the wave dynamics becomes more and more complex, some discrepancies start to appear. For this simulation we used $\Delta x = 0.1$ (m) and $n_k = 0.02$.

Wave profiles at four different times are given in Figure 13. At $t^* = 71.11$ we see the first interaction of the wave front with the still water in the reef flat. An hydraulic jump is originated and a downstream propagating bore is

(19) and the change of variables $w = h + b$ and $q = hu$, we rewrite the hyperbolic system (5) in the conservative form

$$U_t + F(U,b)_x = N(U,b) + M(U,b),$$

with $U = (w,q)^{\mathrm{T}}$,

$$F(U,b) = \left(q, \frac{q^2}{w-b} + \frac{1}{2}g(w-b)^2\right)^{\mathrm{T}}, \quad N(U,b) = (0, -g(w-b)b_x)^{\mathrm{T}}, \text{ and}$$

$$M(U,b) = \left(0, -\frac{1}{2}c_1 \exp\left(c_2\left(\frac{2\pi K_N(w-b)}{T|q|}\right)^{c_3}\right)\frac{1}{(w-b)^2}q|q|\right)^{\mathrm{T}},$$

with $c_1 = 0.00140$, $c_2 = 4.5840$, and $c_3 = 0.1340$. If we use Manning's friction term (18), we get

$$M(U,b) = \left(0, -gn_k^2\frac{1}{(w-b)^{7/3}}q|q|\right)^{\mathrm{T}}.$$

With this notation, the proposed finite volume method takes the form

$$\frac{d}{dt}U_i(t) = -\frac{H_{i+1/2}(t) - H_{i-1/2}(t)}{\Delta x} + N_i(t) + M_i(t), \tag{21}$$

where $U_i(t)$ represents the numerical approximation at $\bar{x}_i$ and $H_{i+1/2}(t)$ are the numerical fluxes

$$H_{i+1/2}(t) = \frac{a^+_{i+1/2}F(U^-_{i+1/2}, b_{i+1/2}) - a^-_{i+1/2}F(U^+_{i+1/2}, b_{i+1/2})}{a^+_{i+1/2} - a^-_{i+1/2}} + \frac{a^+_{i+1/2}a^-_{i+1/2}}{a^+_{i+1/2} - a^-_{i+1/2}}\Big(U^+_{i+1/2} - U^-_{i+1/2}\Big). \tag{22}$$

Here, $U^+_{i+1/2} = \tilde{U}_i(x_{i+1/2})$ and $U^-_{i+1/2} = \tilde{U}_{i+1}(x_{i+1-1/2})$ with $\tilde{U}_i(x)$ defined as

$$\tilde{U}_i(x) = U_i + (U_x)_i(x - \bar{x}_i), \quad x_{i-1/2} < x < x_{i+1/2},$$

where $(U_x)_i$ denotes the numerical derivative calculated with the generalized minmod limiter. In (22), the local propagation speeds $a^{\pm}_{i+1/2}$ are determined by

$$a^+_{i+1/2} = \max\big\{u^+_{i+1/2} + \sqrt{gh^+_{i+1/2}},\, u^-_{i+1/2} + \sqrt{gh^-_{i+1/2}},\, 0\big\},$$

$$a^-_{i+1/2} = \min\big\{u^+_{i+1/2} - \sqrt{gh^+_{i+1/2}},\, u^-_{i+1/2} - \sqrt{gh^-_{i+1/2}},\, 0\big\}.$$

Note that $u = q/h$, therefore to obtain an accurate approximation for u when $h \sim 0$ we use the formula

$$u = \frac{2(w-b)q}{(w-b)^2 + \max((w-b)^2, \epsilon^2)}, \tag{23}$$

with $\epsilon = \min((\Delta x)^4, 1\text{e-}5)$. This formula changes the computation of u only when $h < \epsilon$. Other formulas could be used without affecting the method robustness [30, 8]. At last, the source terms $N_i(t)$ and $M_i(t)$ are approximated by

$$N_i(t) = \left(0, -g\frac{(b_{i+1/2} - b_{i-1/2})((w^-_{i+1/2} - b_{i+1/2}) + (w^+_{i-1/2} - b_{i-1/2}))}{2\Delta x}\right)^{\mathrm{T}}$$

and

$$M_i(t) = \left(0, -\frac{1}{2}c_1 \exp\left(c_2\left(\frac{2\pi K_N(w_i - b_i)|q_i|}{T(q_i^2 + \max(q_i^2, \epsilon^2)}\right)^{c_3}\right) \left(\frac{w_i - b_i}{(w_i - b_i)^2 + \max((w_i - b_i)^2, \epsilon^2)}\right)^2 q_i|q_i|\right)^{\mathrm{T}},$$

or

$$M_i(t) = \left(0, -gn_k^2\left(\frac{w_i - b_i}{(w_i - b_i)^2 + \max((w_i - b_i)^2, \epsilon^2)}\right)^{7/3} q_i|q_i|\right)^{\mathrm{T}},$$

for Manning's friction. Note the use of a formula analogous to (23) to compute $1/(w-b)$ and $1/|q|$. In the following we denote by $\mathrm{Serre}^M_{\alpha,\beta}$ the combination of the proposed model with Manning's friction.

Remark 4.1 This is a second-order accurate scheme that reduces to first-order near non-smooth regions. In some cases it may be necessary to recalculate $w^{\pm}_{i+1/2}$ to guarantee the positivity of the scheme. For ease of presentation, we refer again to [30, 8] for further details. Information about the linear dispersion properties of similar finite difference and finite volume methods can be found in [20, 56].

Now we address the dispersive part (8). We define the approximation points, $x_{i+1} = x_i + \Delta x$, $i = 1, \ldots, N$, with $x_1 = x_L$ and $x_{N+1} = x_R$. Note

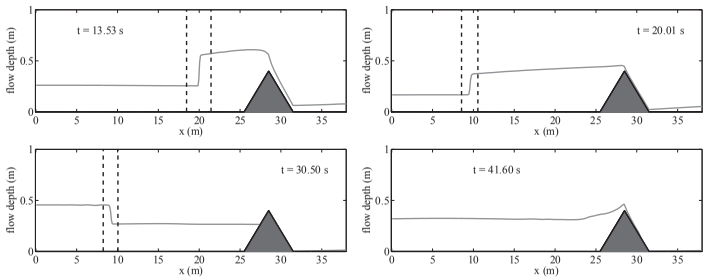

FIGURE 9. Snapshots of the flow propagation in the CADAM project (2000); the area between two dash lines corresponds to breaking regions.

The results of our simulation are given in Figure 8, and they illustrate the good agreement between numerical and experimental data. In Figure 9 we show snapshots of the numerical wave at four different times. The first two images, at $t = 13.53$ (s) and $t = 20.01$ (s), show the wave after interacting with the obstacle. Part of the wave overtakes the obstacle and other part is reflected creating a breaking wave traveling back in the upstream direction. At $t = 30.50$ (s) the breaking wave is now moving in the opposite downstream direction after being reflected in the solid wall at the upstream end. Finally, at $t = 41.60$ (s), the wave is no longer breaking and it is overtaking the triangular obstacle for the second time. For this test we used $\Delta x = 0.1$ (m) and $n_k = 0.01$.

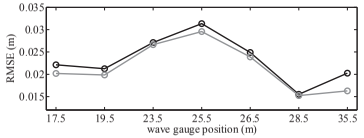

FIGURE 10. Comparison of the RMSE at the seven gauges of the CADAM Project (2000); $\mathrm{Serre}^M_{\alpha,\beta}$ (black line) and $\mathrm{Serre}_{\alpha,\beta}$ (grey line).

In this example, as illustrated in Figure 10, $\mathrm{Serre}_{\alpha,\beta}$ is slightly more accurate than $\mathrm{Serre}^M_{\alpha,\beta}$. The most noticeable difference is at the last gauge, located after the obstacle at $x = 35.5$ (m).

	Mean of Normalized RMSE (%)		
Phase	$\Delta x = 0.1$ (m)	$\Delta x = 0.05$ (m)	$\Delta x = 0.025$ (m)
Run-up	5	5	5
Run-down	4	4	4

TABLE 3. Mean of normalized RMSE in the Synolakis (1987) experiment in function of Δx.

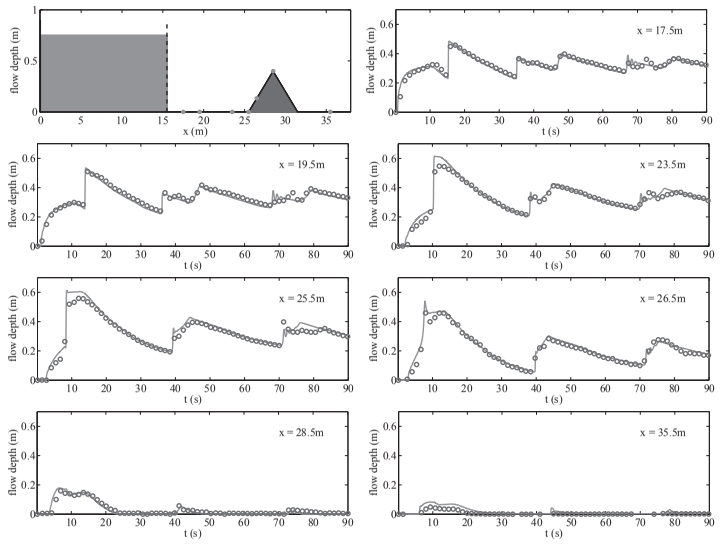

FIGURE 8. The figure in the top left corner shows a schematic representation of the setup used in the CADAM project (2000). The dots indicate the gauges positions. The remaing figures show a comparison between numerical (solid line) and experimental data (dots) at the five gauges.

Figure 8. It consists of a reservoir with a gate located at $x = 15.5$ (m). The initial water depth upstream was 0.75 m and downstream the channel was dry. At time equal zero the gate is open and the water floods the dry portion of the channel interacting with a triangular obstacle. The reservoir is closed at the upstream end and open at the downstream end. To collect data seven gauges were placed across the reservoir.

that these nodes coincide with the finite volume nodes $\bar{x}_{i\pm1/2}$. Since $h_t = 0$, system (8) reduces to the equation

$$(I + T + T^{\alpha,\beta})u_t = g(T - T^{\alpha,\beta})(\eta_x) - Q(u),$$

with T, $T^{\alpha,\beta}$, and Q the differential operators given by (3), (7), and (2), respectively. Applying standard second-order centered finite differences,

$$v_x(x_i) \approx \frac{v_{i+1} - v_{i-1}}{2\Delta x}, \quad v_{xx}(x_i) \approx \frac{v_{i+1} - 2v_i + v_{i+1}}{\Delta x^2}, \quad \text{and}$$

$$v_{xxx}(x_i) \approx \frac{-v_{i-2} + 2v_{i-1} - 2v_{i+1} + v_{i+2}}{2\Delta x^3},$$

we get the system of ordinary differential equations (odes)

$$\frac{d}{dt}u(t) = M_{FD}(u(t)). \tag{24}$$

where M_{FD} denotes a linear finite difference operator (see [16] for details).

The hybrid approach finite difference finite volume means that some relations are required to carry the numerical approximations from one mesh to the other. Whenever necessary we use the following fourth-order approximations,

$$\bar{v}_i = -\frac{1}{24}v_{i-1} + \frac{13}{24}v_i + \frac{13}{24}v_{i+1} - \frac{1}{24}v_{i+2}$$

for the switch from finite difference to finite volume, and

$$v_i = -\frac{1}{12}\bar{v}_{i-2} + \frac{7}{12}\bar{v}_{i-1} + \frac{7}{12}\bar{v}_i - \frac{1}{12}\bar{v}_{i+1}$$

for the switch from finite volume to finite difference.

In the following, reflecting boundary conditions are always assumed. They are implemented considering two additional fictitious nodes at the right and at the left end of the computational domain. At the right we set $u_{N+1} = -u_{N-1}$ and $u_{N+2} = -u_{N-2}$ for the finite difference approximation and $w_N = w_{N-1}$, $w_{N+1} = w_{N-2}$, $q_N = q_{N-1}$, and $q_{N+1} = q_{N-2}$ for the finite volume approximation. At the left end of the domain we proceed similarly. When required, we simulate absorbing boundary conditions by expanding the computational domain by a size large enough.

4.2. Time Discretization. In the time domain $t \in [0, T]$ we consider the time mesh $t_m = t_{m-1} + \Delta t_m$, $m = 1, \ldots, M-1$, with $t_0 = 0$ and $t_M = T$. From the numerical point of view the splitting strategy (9) is approximated by a second-order Strang scheme. Thus, from time level t_{m-1} to t_m the numerical solution associated to $\text{Serre}_{\alpha,\beta}$ is given by

$$(h^m, u^m) = S_{nl}(\Delta t_m/2) \circ S_d^{\alpha,\beta}(\Delta t_m) \circ S_{nl}(\Delta t_m/2)(h^{m-1}, u^{m-1}).$$

After the spatial discretization $S_{nl}(\cdot)$ and $S_d^{\alpha,\beta}(\cdot)$ refer to the systems of odes (21) and (24), respectively.

To solve (24) we use a second-order strong stability preserving Runge-Kutta method [22]. For the generic odes system

$$\frac{d}{dt} w(t) = L(w(t)),$$

it is defined by

$$\begin{aligned} w^{(1)} &= w^m + \Delta t_m L(w^m) \\ w^{m+1} &= \frac{1}{2} w^m + \frac{1}{2} w^{(1)} + \frac{1}{2} \Delta t_m L(w^{(1)}). \end{aligned}$$

For the system of odes related with the hyperbolic part (21) we resort to a new class of semi-implicit Runge-Kutta methods [7]. This class of methods is specifically design for odes systems of the form

$$\frac{d}{dt} w(t) = F(w(t)) + G(w(t))w(t), \tag{25}$$

where $F(w(t))$ and $G(w(t))$ represent a non-stiff and a possibly stiff term, respectively. These methods treat the non-stiff term $F(w(t))$ explicitly and the stiff term $G(w(t))w(t)$ in a mixed way, $G(w(t))$ explicitly and $w(t)$ implicitly. Note that (21) can be written in the form (25) and the stiffness arises in the friction term $M(t)$ when $h \to 0$. As detailed in [7] this new class of semi-implicit schemes has the advantage of preserving the positivity of the spatial discretization. It is also simpler to implement when compared with traditional implicit schemes that treat the term $G(w(t))w(t)$ implicitly. Moreover, like in the implicit ones, the associated time step restriction depends only on the explicit discretization of the non-stiff term $F(w(t))$. For

at all times. The results with $\text{Serre}_{\alpha,\beta}^M$ are also given, and they show that the Manning's friction formula is less accurate.

Snapshots of the run-down phase are given in Figure 7. Again, we can observe a good agreement between numerical simulation and experimental data.

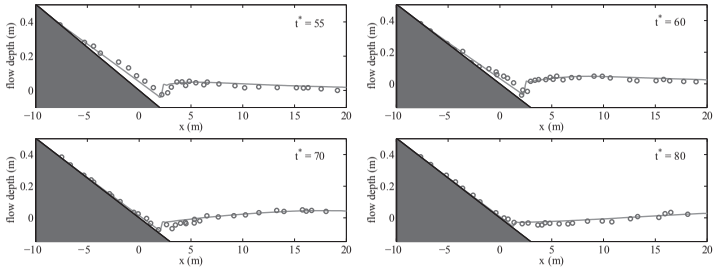

FIGURE 7. Comparison between numerical (solid line) and experimental data (dots) at four different times for the run-down phase of the Synolakis (1987) experiment.

The normalized RMSE for the run-down phase is given in Table 2. For this phase $\text{Serre}_{\alpha,\beta}$ and $\text{Serre}_{\alpha,\beta}^M$ achieved a similar performance. We note that the NTHMP benchmark test did not include the run-down phase.

	Run-down Phase - Normalized RMSE (%)				
	$t^* = 55$	$t^* = 60$	$t^* = 70$	$t^* = 80$	Mean
$\text{Serre}_{\alpha,\beta}$	5	5	3	3	4

TABLE 2. Normalized RMSE for $\text{Serre}_{\alpha,\beta}$ with respect to the Synolakis (1987) experiment.

In Table 3 we analyze the sensitivity of our implementation to the mesh size Δx. The same mean of normalized RMSE for the run-up and run-down phases prove the robustness against this parameter.

5.2.2. *CADAM Project* [34] - *Dam break flow over a triangular hump.* The CADAM (Concerted Action on Dambreak Modelling), was a European project whose main goal was to push forward the numerical simulation of dam break events [34, 28]. During the project duration a database of tests cases was created. One of such tests cases is shown in the top left image of

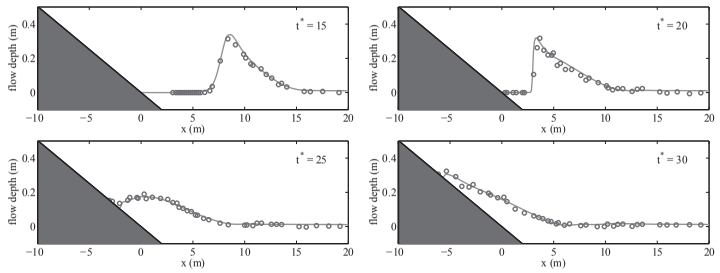

FIGURE 5. Comparison between numerical (solid line) and experimental data (dots) at four different times for the Synolakis (1987) experiment.

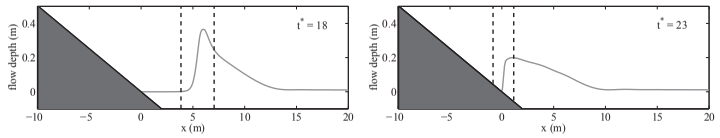

FIGURE 6. Snapshots of the soliary wave propagation in the Synolakis (1987) experiment; the area between two dash lines corresponds to breaking regions.

series of pre-established tests were approved for tsunami inundation modeling. One of the benchmark tests was based on the Synolakis (1987) experiment. The models had to achieved a normalized root-mean-squared-error (RMSE) smaller than 10% at the times shown in Figure 5. In Table 1 we compare the error of our approach with the average error of the approved models. As can be seen, the error of our $\text{Serre}_{\alpha,\beta}$ is bellow the average error

	Run-up Phase - Normalized RMSE (%)				
	$t^* = 15$	$t^* = 20$	$t^* = 25$	$t^* = 30$	Mean
$\text{Serre}_{\alpha,\beta}$	3	8	6	3	5
$\text{Serre}^M_{\alpha,\beta}$	4	10	5	3	6
NTHMP	7	9	6	4	7

TABLE 1. Comparison of the normalized RMSE with respect to the Synolakis (1987) experiment; proposed $\text{Serre}_{\alpha,\beta}$, $\text{Serre}^M_{\alpha,\beta}$, and mean of the four models presented in NTHMP (2012).

(25), the adopted semi-implicit second-order method reads

$$
\begin{aligned}
w^{(1)} &= \frac{w^m + \Delta t_m F(w^m)}{1 - \Delta t_m G(w^m)} \\
w^{(2)} &= \frac{3}{4} w^m + \frac{w^{(1)} + \Delta t_m^{(1)} F(w^{(1)})}{4(1 - \Delta t_m^{(1)} G(w^{(1)}))} \\
w^{(3)} &= \frac{1}{3} w^m + \frac{2(w^{(2)} + \Delta t_m^{(2)} F(w^{(2)}))}{3(1 - \Delta t_m^{(2)} G(w^{(2)}))} \\
w^{m+1} &= \frac{w^{(3)} - (\Delta t_m)^2 F(w^{(3)}) G(w^{(3)})}{1 + (\Delta t_m G(u^{(3)}))^2}.
\end{aligned} \tag{26}
$$

For our finite volume method the Courant-Friedrich-Lvy (CFL) time step stability condition is given by

$$
\Delta t_m \leq \frac{\Delta x}{2a}, \quad \text{with } a = \max_i \{a^+_{i+1/2}, -a^-_{i+1/2}\}. \tag{27}
$$

In (26), the notation $\Delta t_m^{(j)}$ refers to the CFL condition associated with $w^{(j)}$, $j = 1, 2$. To ensure the positivity of the solution the time step Δt_m needs to satisfy $\Delta t_m \leq \Delta t_m^{(j)}$, $j = 1, 2$. Otherwise, we have to restart the time scheme with $\Delta t_m = k \Delta t_m^{(1)}$ (or $\Delta t_m = k \Delta t_m^{(2)}$), with $k \in (0, 1)$; we used $k = 0.9$.

5. Numerical Experiments

In this section we test our model as well as the proposed numerical implementation. We use a problem with known theoretical solution and several laboratory experiments. The laboratory experiments are divided in two groups: weakly dispersive waves and strongly dispersive waves.

In all the following experiments, and when friction is considered, the Manning coefficient is equal to 0.01 ($\text{m}^{-1/3}\text{s}$) or 0.02 ($\text{m}^{-1/3}\text{s}$). These are common values for the roughness of glass-type or concrete surfaces like the ones used in the experiments reported in this paper [20, 25, 40]. Regarding the breaking parameters, their estimation a priori is an unsolved problem and they have to be individually adjusted in order to reflect the particular characteristics of each experiment. Nevertheless, the values used in the following sections are similar to many values found in the literature [20, 25, 48, 29]. In what concerns the dispersion parameters α and β their optimal value is also problem dependent. Based on our experimental work, the combination

$(\alpha, \beta) = (0.04, 0.07)$ seems to be a good initial guess. Some attempts have been made to estimate the optimal values of the dispersion parameters associated with improved Serre-type systems, see e.g., [14, 3]. However, the analysis is not problem-independent and several restrictions are made.

5.1. Solitary wave propagation. We start our numerical experiments with the propagation of a solitary wave over a flat bottom. For this simple case we can obtain an analytic solution for $\text{Serre}_{\alpha,\beta}$ with α and β equal to zero, which corresponds to classical Serre. The solution is given by

$$h(x,t) = h_0 + a(\text{sech}(K(x - Ct - x_0)))^2, \quad u = C(1 - h_0/h),$$

where a is the wave amplitude, x_0 is the initial position of the wave crest, $K = \sqrt{3a/(4h_0^2(h_0 + a))}$, and $C = c_0\sqrt{1 + a/h_0}$, with $c_0 = \sqrt{gh_0}$.

We use this example to illustrate the convergence rate of our numerical scheme. We define the domain $[0, 100]$ (m) and the constants $h_0 = 1$ (m), $a = 0.5h_0$, and $x_0 = 20$ (m). We run the simulation until $T = 15$ (s) using successively smaller mesh sizes, namely, $\Delta x = 0.2$ (m), $\Delta x = 0.1$ (m), $\Delta x = 0.05$ (m), and $\Delta x = 0.025$ (m). To measure the error we use the discrete L^∞ norm $\|\cdot\|_\infty$. We denote by E_η and E_u the difference between the numerical solution and the theoretical solution of η and u, respectively. Like in the following sections, the time step is fixed by the CFL condition (27).

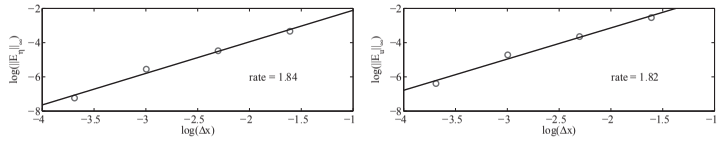

FIGURE 3. Solitary wave propagation over a flat bottom. Estimated convergence rate for η (in the left) and for u (in the right). The solid line represents the best fitting least square line.

In Figure 3 we plot the $\log(\|E_\eta\|_\infty)$ and $\log(\|E_u\|_\infty)$ versus $\log(\Delta x)$. The convergence rate is estimated by the slope of the best fitting least square line. The values obtained are 1.84 for η and 1.82 for u. For this smooth example these values are in close agreement with the expected second order convergence rate.

5.2. Weakly dispersive waves. The next set of experiments illustrates the ability of our approach to accurately simulate wave breaking and propagation over dry areas. We focus on weakly dispersive waves, meaning that the parameters α and β are set to zero. In all examples we use the breaking parameters $\phi_i = 0.5$ and $\phi_f = 0.4$. The parameter F_f was not considered.

Also presented is a comparison between the results obtained with Manning's friction formula (18) and those obtained with the proposed one (19). To perform this comparison we first tuned the Manning's friction coefficient n_k. Afterwards, we used formula (20) to obtain the corresponding value of the parameter K_N. No attempt was made to optimize K_N or the parameters c_1, c_2, and c_3 arising in (19).

5.2.1. *Synolakis* [46] *- Solitary wave run-up and run-down over a sloping beach.* Our first experiment refers to the run-up and run-down of a breaking solitary wave over a slopping beach [46]. The experimental setup is given in Figure 4, it shows the beach with a slope of 1 : 19.85 and the still water depth $h_0 = 1$ (m).

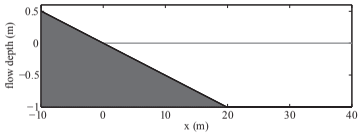

FIGURE 4. Schematic representation of the setup used in the experiment of Synolakis (1987). The horizontal grey line corresponds to the initial still water depth, $h_0 = 1$ (m).

The solitary wave with amplitude $a = 0.3$ (m) is initially centered around $x_0 = 25.5$ (m). Simulations were performed with $\Delta x = 0.1$ (m) and Manning's coefficient $n_k = 0.02$. Snapshots of the wave at the time $t^* = t\sqrt{g/h_0}$ are given in Figure 5. They show the wave propagating before breaking, at $t^* = 15$, the breaking phase, at $t^* = 20$, and the run-up phase, at $t^* = 25$ and $t^* = 30$. A good agreement between numerical simulation and experimental data is observed in all phases.

The breaking phase occurs approximately between $t^* = 18$ and $t^* = 23$. This is well predicted by our model and is illustrated in Figure 6.

In 2012 the US National Tsunami Hazard Mitigation Program (NTHMP) conducted a model benchmarking workshop [35]. The models that passed a